Supplementary information for "Nodal superconductivity in miassite $Rh_{17}S_{15}$"

Hyunsoo Kim,[1,2,*] Makariy A. Tanatar,[1,2] Marcin Kończykowski,[3] Udhara S. Kaluarachchi,[1,2] Serafim Teknowijoyo,[1,2] Kyuil Cho,[1] Aashish Sapkota,[1] John M. Wilde,[1,2] Matthew J. Krogstad,[4] Sergey L. Bud'ko,[1,2] Philip M. R. Brydon,[5] Paul C. Canfield,[1,2] and Ruslan Prozorov[1,2,†]

[1]*Ames National Laboratory, Iowa State University, Ames, Iowa 50011, USA*
[2]*Department of Physics & Astronomy, Iowa State University, Ames, Iowa 50011, USA*
[3]*Laboratoire des Solides Irradiés, CNRS UMR 7642 & CEA-DSM-IRAMIS, École Polytechnique, F-91128 Palaiseau cedex, France*
[4]*Materials Science Division, Argonne National Laboratory, Lemont, Illinois 60439, USA*
[5]*Department of Physics and MacDiarmid Institute for Advanced Materials and Nanotechnology, University of Otago, P.O. Box 56, Dunedin 9054, New Zealand*

(Dated: June 16, 2023)

I. ELECTRON IRRADIATION

The low-temperature 2.5 MeV electron irradiation was performed at the SIRIUS Pelletron facility of the Laboratoire des Solides Irradiés (LSI) at the Ecole Polytechnique in Palaiseau, France. The acquired irradiation dose is conveniently expressed in C/cm^2 and measured directly as a total charge accumulated behind the sample by a Faraday cage. Therefore, 1 C/cm^2 $\approx 6.24 \times 10^{18}$ electrons/cm^2. The irradiation was carried out with the sample immersed in liquid hydrogen at about 20 K. Low-temperature irradiation is needed to slow down the recombination and migration of defects. Upon warming up to room temperature, a quasi-equilibrium population of atomic vacancies remains due to a substantial difference in the migration barriers between vacancies and interstitials. An example of such incremental irradiation/measurement sequence showing the resistivity change measured in-situ, as well as the annealing after warming up, is given elsewhere [1]. In the present case, the sample was dispatched between the lab and the irradiation facility for the measurements and irradiation, and then the sequence was repeated. Further information on the physics of electron irradiation can be found elsewhere [2, 3].

II. ELECTRICAL TRANSPORT MEASUREMENT

Four-probe electrical resistivity measurements were performed in *Quantum Design* PPMS on three samples S-2, S-3, and S-4. Contacts to the samples were soldered with tin [4] and had resistance in mΩ range. Electrical resistivity at room temperature was determined as 130$\pm$20 $\mu\Omega$ cm, based on the average of three samples. The same samples with contacts were measured before and after electron irradiation, excluding the uncertainty of the geometric factor determination.

III. TUNNEL DIODE RESONATOR TECHNIQUE

The temperature variation of London penetration depth was measured in a ^{3}He cryostat and a dilution refrigerator (DR) by using a TDR technique [5]. A small sample typically < 0.8 mm in the longest dimension was mounted on a sapphire rod with a diameter of 1 mm and inserted into a 2 mm inner diameter copper coil that produces rf excitation field with empty-resonator frequency of 14.5 MHz and 16.6 MHz for ^{3}He-TDR and DR-TDR, respectively, with amplitude $H_{ac} \approx 20$ mOe. The shift of the resonant frequency (in cgs units), $\Delta f(T) = -G4\pi\chi(T)$, where $\chi(T)$ is the differential magnetic susceptibility, $G = f_0 V_s/2V_c(1-N)$ is a constant, N is the demagnetization factor, V_s is the sample volume and V_c is the coil volume. The constant G was determined from the full frequency change by physically pulling the sample out of the coil. With the characteristic sample size, R, $4\pi\chi = (\lambda/R)\tanh(R/\lambda) - 1$, from which $\Delta\lambda$ can be obtained [5, 6].

IV. X-RAY DIFFRACTOMETRY

The high-energy X-ray diffraction measurements were performed at station 6-ID-D at the Advanced Photon Source, Argonne National Laboratory. The use of X-rays with an energy of 100 keV minimizes sample absorption and allows to probe of the entire bulk of the sample using an incident beam with a size of 0.5$\times$0.5 mm^2, over-illuminating the sample. The samples were held on Kapton tape in a Helium closed-cycle refrigerator and Helium exchange gas was used. Extended regions of selected reciprocal lattice planes were recorded by a MAR345 image plate system positioned 1585 mm behind the sample as the sample was rocked through two independent angles up to $\pm 2.0^\circ$ about axes perpendicular to the incident beam.

---

* Present affiliation: Department of Physics, Missouri University of Science and Technology, Rolla, Missouri 65409, USA
† corresponding author: prozorov@ameslab.gov

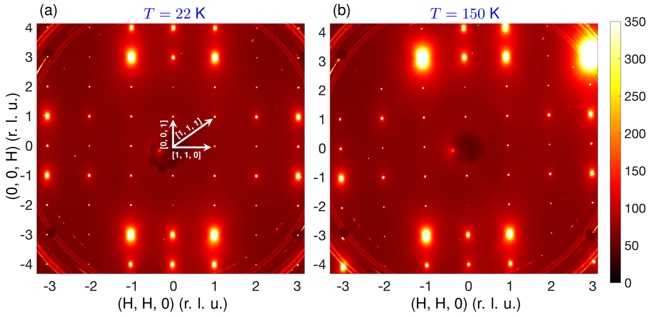

FIG. S1. Results of high-energy X-ray diffraction measurements showing extended regions of (H,H,0)- (0,0,H) reciprocal planes at two temperatures 22 (left) and 150 K (right). Intensities in each panel are color coded to a linear scale. Small circular black circles at f3, 3, 3g Bragg peaks and around the beam center (in panel ̈) are from the lead masks which were used to mask the intense Bragg peaks to avoid the oversaturation of the detector pixels. Furthermore, the polycrystalline rings are from the Be domes. In panel b, the large intensity at (3, 3, 3) peak is due to the lead mask not being at the correct position. Also, the higher intensity for (-1, -1, 3) Bragg peak in comparison to (-1 -1 -3) and missing (-2, -2, 3) peak are due to the crystal being slightly misaligned at 150 K. The strong regular lattice peaks were partially blocked/saturated to enable resolution in 10^{-4} to 10^{-5} range. No additional superstructure peaks corresponding to CDW were observed at low temperatures within this resolution.

V. TRANSPORT PROPERTIES

The cross-over maximum in $\rho(T)$ at around 100 K may be caused by the contribution of two types of carriers with very different properties, as usually discussed for materials with Matthiessen's rule violation [7–9] in "parallel resistor" model. The crossover in resistivity is accompanied by the sign change of the Hall effect [10, 11]. The large magnitude of the Hall constant at low temperatures suggests that low carrier density electrons dominate transport near T_c [10]. Estimate from single band model, $R_H = 1/(ne)$, the carrier density $n \approx 3 \times 10^{20}$ cm^{-3} provides an upper bound [10]. Use of the two-carrier type analysis of the field and temperature-dependent Hall effect and magnetoresistance suggest that electron carrier density is in fact notably lower, $\sim 1 \times 10^{19}$ cm^{-3} and the mobility of these carriers is quite high, in 600 cm^{2}V^{-1}s^{-1} range, indicating small effective mass of the carriers [11]. These high mobility electronic carriers are clearly inconsistent with rather high specific heat Sommerfeld γ, a high value of heat capacity jump at T_c, and the high upper critical fields. This may be suggesting that holes, dominating the Hall effect at high temperatures, should be notably heavier. The two-band character of the transport clearly reveals itself in response to electron irradiation. The contribution of small carrier density high mobility carriers suffers two times stronger from the introduction of disorder [12], giving an increase in the difference plot on cooling. The two-band charge transport needs to be accounted for properly for the estimation of the scattering rate, introduced by irradiation. We adopted resistivity variation at low and high temperatures as an uncertainty of the scattering rate determination.

VI. RUTGERS RELATION

The heat capacity jump is $\Delta C/T = 0.24$ J/mol K^2 [10, 13]. Note we used the lattice parameter of 9.911 Å[14] for conversion of the heat capacity jump. The slope is determined to be $H'_{c2}(T_c) = -6.78$ T/K by fitting data points between $0.87T_c$ and T_c [13]. Choice of $\lambda(0) = 550$ nm gives good agreement between experiment and the Rutgers' relation where $\rho'_s(1) = -1.11$.

VII. UPPER CRITICAL FIELD DETERMINATION

The upper critical fields were determined from resistive measurements. In Fig. S2 we show temperature-dependent resistivity measured in magnetic fields applied along [100] crystallographic direction transverse to the electrical current. The top panel shows results for the pristine sample, bottom panel for the sample with 0.912 C/cm^2 irradiation. Resistive transitions remain sharp with the application of magnetic fields and do not show significant broadening. We used the onset criterion for T_c determination. These H_{c2} determinations are in good agreement with the upper critical fields determined from heat capacity measurements in which equal entropy construction was used for the determination of both T_c and $H_{c2}(T)$ [13]. The resistivity onset curve practically coincides with the heat capacity curve, see Fig. 3a in the main text.

VIII. SUPERCONDUCTING STATE

Having established the angular dependence of the order parameter, $\Omega(\varphi, \theta)$, we can now solve the Eilenberger self-consistency equation for the temperature-dependent part, $\Psi(t)$, to obtain the superconducting gap function $\Delta = \Psi\Omega$. Details of the calculations of this and other thermodynamic quantities are described in detail elsewhere Ref.[5, 15]. For comparison, the application of this approach to MgB_2 superconductor is shown in Ref.[16].

A. Extended s-wave pairing state

The angular-dependent part of the order parameter for the extended s-wave gap proposed in the paper is

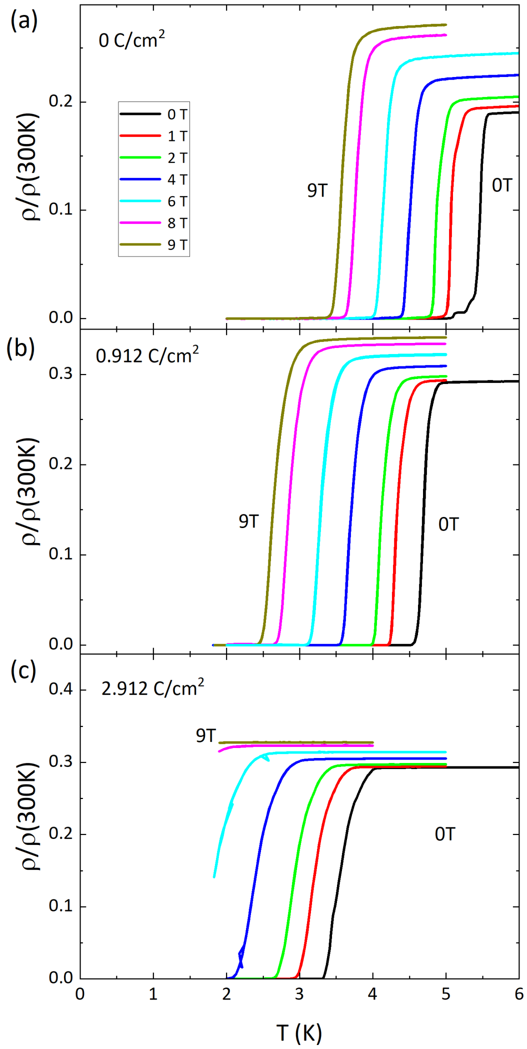

FIG. S2. Temperature dependent resistivity of pristine (a) 0 C/cm^2, and electron irradiated samples (b) 0.912 C/cm^2 and (c) 2.912 C/cm^2 of $Rh_{17}S_{15}$ in magnetic fields 0T, 1 T, 2 T, 4T, 6T, 8 T and 9 T (right to left). The magnetic field was applied transverse to the current and along [100] crystallographic direction.

$$\Omega(\theta,\phi) \;=\; C_r\left[r+(1-|r|)\left(\cos^4\theta + \sin^4\theta[\sin^4\varphi+\cos^4\varphi]\right)\right] \tag{S1}$$

where the normalization constant

$$C_r = \sqrt{\frac{105}{41+126r+146r^2-2(41+63r)|r|}} \tag{S2}$$

ensures that $\int|\Omega(\theta,\phi)|^2 d\Omega = 4\pi$. The key evolution of $\Omega(\theta,\phi)$ with r is shown in fig. S3, At $r=-1$, the form factor gives isotropic s-wave pairing. Increasing r, gap minima develop along the crystal axes [panel (a)]. At $r=-0.5$ this deepens to a quadratic point node; further increasing r this point node develops into a circular line node centered around the crystal axes [panels (b) and (c)]. These grow with r until they touch at the critical value of $r_{\text{crit}} = \frac{1}{3}$ [panel (d)]. Further increasing r the line nodes recombine into eight circular line nodes about the cubic body diagonals [panel (e)]. Increasing r beyond -0.25 these nodes collapse down to quadratic points, and then eventually give rise to an anisotropic fully-gapped state with gap minima along the cubic body diagonals [panel (f)].

B. Thermodynamic quantities

Figure S4 summarizes the temperature dependence of the calculated superconducting gap, heat capacity, and superfluid density for our order parameter with $r=-0.45$, shown by the red solid curves. For comparison, other usual cases are shown on all frames. Notice the difference between 2D s-wave, $\sim\cos(2\varphi)$, and 3D s-wave, $\sim\cos(2\varphi)\sin^2(\theta)$. Interestingly, panel (a) shows that the maximum gap value for our order parameter is less than that in typical s-and d-wave gap symmetries. Unfortunately, we are not aware of the direct measurements of the gap $Rh_{17}S_{15}$, and the maximum gap value is unknown. On the other hand, the gap estimated from thermodynamic measurements only provides the Fermi

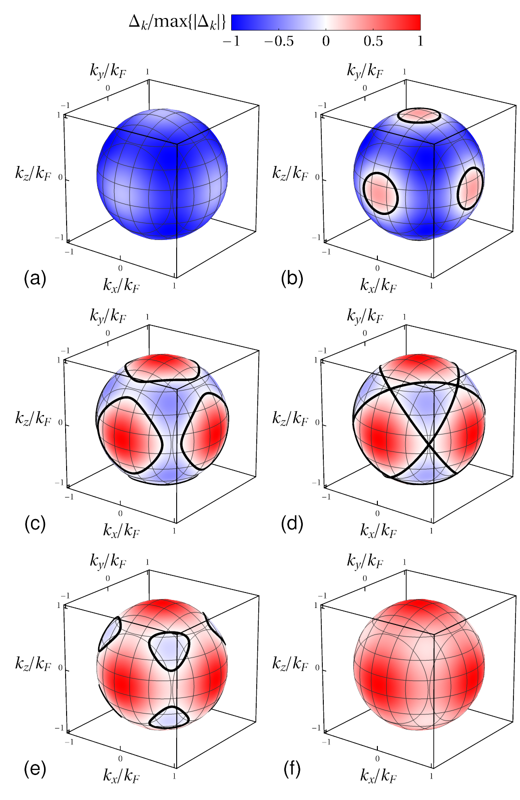

FIG. S3. Extended s-wave gaps for (a) $r=-0.55$, (b) $r=-0.45$, (c) $r=-0.35$, (d) $r=r_{\text{crit}}=-\frac{1}{3}$, (e) $r=-0.3$, and (f) $r=-0.2$.

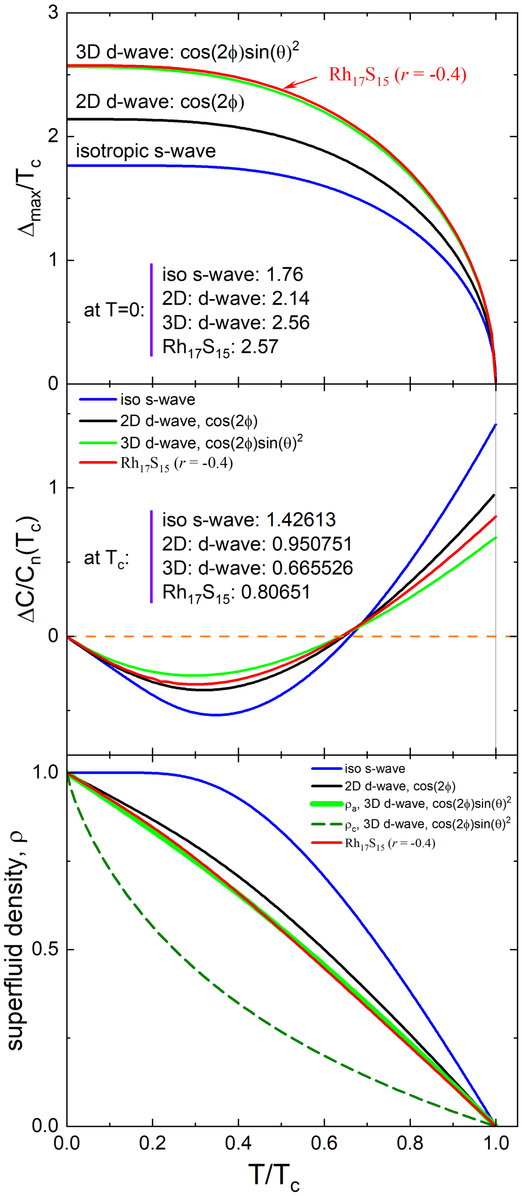

FIG. S4. Temperature evolution of (a) superconducting gap, (b) heat capacity, and (c) superfluid density in $Rh_{17}S_{15}$ (red solid lines), compared to isotropic s-wave and 2D and 3D d-wave symmetries.

surface average.

In panel (b) we plot the temperature dependence of the predicted deviation of the specific heat from the normal state, i.e. $\Delta C/C_n = (C_s - C_n)/C_n$, with $C_n = \gamma T$. For all nodal gaps the predicted heat capacity jump at T_c [$\Delta C(T_c)$] is smaller than the BCS weak-coupling value of 1.43, since the condensation energy is maximal for an isotropic s-wave gap. In contrast, the reported experimental heat-capacity jump is nearly 2 [10]. High ratios of $\Delta C/C_n > 2$ have been found in heavy fermion compounds, namely $CeCoIn_5$, $CeRhIn_5$, U_6Fe, UBe_{13}, $PrOs_4Sb_{12}$, $NpPd_5Al_2$ (see Ref. [17] for review). The origin of these high heat capacity jumps is not well understood, but exceeding the weak-coupling value is typically associated with strong-coupling superconductivity; performing a strong-coupling calculation for $Rh_{17}S_{15}$is far beyond the scope of the current work. Naren *et al.* suggest the Sommerfeld coefficient $\gamma \approx 100$ mJ/mol K^2 in $Rh_{17}S_{15}$ is larger than that of conventional metals possibly due to a narrow Rh-d band consistent with the observed high $H_{c2}(0)$ indicating heavy effective mass, and the shoulder-like feature around 100 K in the resistivity is associated with the formation of the narrow band [10]. However, the response of the resistivity to disorder revealed the disobeyed Matthiessen rule below 100 K, suggesting the absence of activation that is expected for narrow band contribution.

In panel (c), we compare the calculated superfluid density in various gap symmetries. The superfluid density $Rh_{17}S_{15}$ is remarkably well reproduced by an in-plane component of a 3D d-wave. We note that there are no free parameters here. However, since this gap belongs to the two-dimensional E_g irrep, it lowers the symmetry of the electronic dispersion from cubic to tetragonal, implying a nematic superconducting state. This is a highly exotic scenario, as nematic superconductivity has so far only been observed in the Bi_2Se_3 family [18]. The nematicity is reflected in the superfluid density which shows stark differences between the in-plane and c-axis directions.

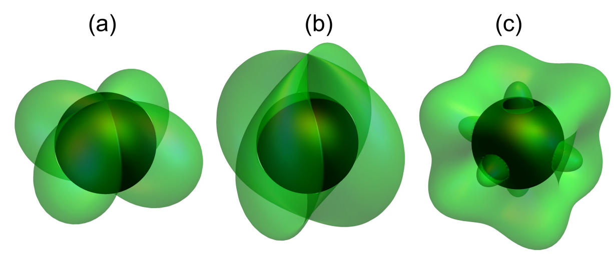

FIG. S5. Possible superconducting gap on a spherical Fermi surface (dark green) relevant for $Rh_{17}S_{15}$. (a) 3D d-wave, $\cos(2\phi)\sin^2\theta$. (b) 2D d-wave, $\cos(2\phi)$. Clearly, the 2D case is impossible because it results, mathematically, in a 4-fold degenerate vertical line node not residing on any Fermi surface. Panel (c) is for the extended s-wave with accidental nodes (see Eq. S1).

[1] R. Prozorov, M. Kończykowski, M. A. Tanatar, A. Thaler, S. L. Bud'ko, P. C. Canfield, V. Mishra, and P. J. Hirschfeld, Phys. Rev. X **4**, 041032 (2014).

[2] A. Damask and G. Dienes, Point Defects in Metals (Gordon and Breach, 1963).

[3] M. Thompson, Defects and Radiation Damage in Metals,

Cambridge Monographs on Physics (Cambridge University Press, 1969).
[4] M. A. Tanatar, N. Ni, S. L. Bud'ko, P. C. Canfield, and R. Prozorov, Superconductor Science and Technology **23**, 054002 (2010).
[5] R. Prozorov and V. G. Kogan, Reports on Progress in Physics **74**, 124505 (2011).
[6] R. Prozorov and R. W. Giannetta, Superconductor Science and Technology **19**, R41 (2006).
[7] J. Bass, Advances in Physics **21**, 431 (1972).
[8] E. H. Sondheimer and A. H. Wilson, Proceedings of the Royal Society of London. Series A. Mathematical and Physical Sciences **190**, 435 (1947).
[9] P. B. Allen, in Superconductivity in d- and f-Band Metals, edited by H. Suhl and M. B. Maple (Academic Press, 1980) pp. 291–304.
[10] H. R. Naren, A. Thamizhavel, A. K. Nigam, and S. Ramakrishnan, Phys. Rev. Lett. **100**, 026404 (2008).
[11] R. Daou, D. Berthebaud, and A. Maignan, Journal of Physics: Condensed Matter **29**, 075604 (2016).
[12] E. C. Blomberg, M. A. Tanatar, A. Thaler, S. L. Bud'ko, P. C. Canfield, and R. Prozorov, Journal of Physics: Condensed Matter **30**, 315601 (2018).
[13] M. Uhlarz, O. Ignatchik, J. Wosnitza, H. Naren, A. Thamizhavel, and S. Ramakrishnan, Journal of Low Temperature Physics **159**, 176 (2010).
[14] S. Geller, Acta Cryst. **15**, 1198 (1962).
[15] V. G. Kogan, C. Martin, and R. Prozorov, Phys. Rev. B **80**, 14507 (2009).
[16] H. Kim, K. Cho, M. A. Tanatar, V. Taufour, S. K. Kim, S. L. Bud'ko, P. C. Canfield, V. G. Kogan, and R. Prozorov, Symmetry (Basel). **11**, 1012 (2019).
[17] B. White, J. Thompson, and M. Maple, Physica C: Superconductivity and its Applications **514**, 246 (2015).
[18] K. Matano, M. Kriener, K. Segawa, Y. Ando, and G.-q. Zheng, Nature Physics **12**, 852 (2016).